# Pressure-induced superconductivity in the weak topological insulator BiSe

Pallavi Malavi [1],[*] Arpita Paul,[2] Achintya Bera [1], D. V. S. Muthu [1], Kunjalata Majhi,[1] P S Anil Kumar,[1] Umesh V. Waghmare [2], A. K. Sood,[1] and S. Karmakar [3],[†]

[1]*Department of Physics, Indian Institute of Science, Bangalore 560012, India*
[2]*Theoretical Sciences Unit, Jawaharlal Nehru Centre for Advanced Scientific Research, Bangalore 560064, India*
[3]*HP&SRPD, Bhabha Atomic Research Centre, Trombay, Mumbai 400085, India*

Layered BiSe in the trigonal $P\bar{3}m1$ phase is a weak topological insulator and a candidate topological crystalline insulator. Here using structural, spectroscopic, resistance measurements at high pressure and density functional theory calculations, we report that BiSe exhibits a rich phase diagram with the emergence of superconductivity above 7 GPa. Structural transitions into SnSe-type energetically tangled orthorhombic structures and, subsequently, into a CsCl-type cubic structure having distinct superconducting properties are identified at 8 and 13 GPa, respectively. Superconductivity is preserved as the system transforms back to the trigonal phase upon release of pressure. Spin-orbit coupling plays a significant role in enhancement of $T_c$ in the trigonal and cubic phases. In the orthorhombic $Cmcm$ phase, $T_c$ decreases monotonically with increasing pressure, whereas unusual pressure-independent $T_c$ is observed in the cubic $Pm\bar{3}m$ phase. Theoretical analysis reveals topological surface states in the cubic phase. The emergence of superconductivity within the topological phases makes BiSe a candidate topological superconductor.

The search for superconductivity in various types of topological quantum materials has been of immense current research interest for the possible exploration of Majorana quasiparticles in condensed matter physics and for potential applications in topological quantum computation [1,2]. Among these, three-dimensional (3D) topological insulators (TIs) are characterized by nontrivial $Z_2$ band topology due to the presence of strong spin-orbit coupling (SOC) and time-reversal symmetry (TRS) invariant and exhibit spin-polarized metallic surface states forming a Dirac cone. These are further classified as either strong (STI) or weak (WTI) topological insulators based on the TRS invariant criteria. In a STI, TRS protects the surface states on all surfaces with an odd number of Dirac cones, whereas a WTI is considered as stacking of 2D TI layers and thus the surface states occur only on the side surfaces with even number of Dirac cones and the layer surface remains insulating [3–10]. Topological crystalline insulators (TCIs) are another class with nontrivial band topology where conducting surface states with even number of Dirac cones are protected by crystal mirror symmetry without the need for SOC [11–13]. Most weak topological insulators are also candidates for TCIs having gapless states on the layered surfaces [8,14,15], making them candidates for higher-order topological insulators [16,17].

Superconductivity (SC) in 3D TIs has been observed by the proximity effect, chemical doping, as well as under pressure [18–22]. Cu-intercalated highly doped $Bi_2Se_3$ exhibits unconventional bulk SC with Andreev bound states on its surface, characterizing a topological SC state [20,21]. Efforts to induce SC at high pressure to obtain clean 3D topological SC without doping often lead to structural transitions into topologically trivial metallic phases prior to the emergence of SC [22,23]. Searching for SC in diverse TIs, including WTIs, is thus of tremendous current interest. Recently, bismuth-bilayer sandwiched $Bi_2Se_3$, $Bi_2Te_3$, and BiTeI superlattice structures are reported to exhibit coexisting WTI and TCI states [8,14,16,24], and are promising candidates to exhibit intriguing topological properties also at high pressure.

Here we report structural, vibrational, and resistance measurements at high pressure and density functional theory calculations on BiSe, a natural superlattice of $Bi_2Se_3 - Bi_2 - Bi_2Se_3$ unit. The ambient trigonal phase ($P\bar{3}m1$) undergoes an isostructural transition at ∼3 GPa, followed by a total structural reconstruction above 8 GPa into SnSe-type orthorhombic structures, with energetically tangled mixed phases ($Cmcm$ and $Pnma$). At pressures above 13 GPa, a CsCl-type cubic phase ($Pm\bar{3}m$) is stabilized. With increasing pressure, the signature of filamentary SC onset has been noticed within the trigonal phase at ∼6 GPa, although zero resistance has been detected above ∼8.5 GPa. Upon release of pressure, BiSe transforms back to the trigonal structure that supports WTI and TCI states and, more importantly, SC is preserved in the pressure-released sample, with $T_c$ significantly enhanced compared to the theoretically estimated value. The presence of strong SOC in the trigonal phase is clearly evident from the observed weak antilocalization cusp in the magneto-resistance measurements. In the mixed phase region at the trigonal-orthorhombic structural transition, the inhomogeneity of emerged SC phases is evident from the observed

———————
[*]Present address: HP&SRPD, Bhabha Atomic Research Centre, Mumbai 400085, India.
[†]sdak@barc.gov.in

resistance peak at the SC onset and two-step transition. The onset $T_c$ of the *Cmcm* phase shows a dome-shaped $p$ dependence, whereas unusual $p$-independent $T_c$ is observed in the cubic phase. Our *ab initio* surface-state calculations have revealed a linear band crossing (Dirac band) on the (001) surface of the cubic BiSe phase, predicting the topological semimetal state.

High-quality single crystals of BiSe were synthesized by the modified Bridgman method, as described elsewhere [24]. X-ray diffraction (XRD) measurements at high pressure are performed at the XPRESS beam line of the Elettra synchrotron with Au as the x-ray pressure marker. Raman spectra from a BiSe single crystal are recorded using the HORIBA Jobin Yvon (HR-800) Raman spectrometer. Diamond Anvil Cell (DAC)-based resistance and magneto-resistance (MR) measurements have been performed on single crystals (dimension $\sim 100 \times 100 \times 20$ μm), using the standard four-probe method (with 4-μm-thick Pt leads to make electrical contacts with the sample in the van der Pauw geometry) and by the ac lock-in detection technique. For measurements down to 1.4 K, the DAC (Stuttgart version) is mounted inside a KONTI-IT (Cryovac) cryostat. A nonmagnetic Cu-Be DAC (Easylab) is used for MR, Hall resistance, and dc-magnetic susceptibility measurements using a superconducting quantum interference device (SQUID) magnetometer (Cryogenic Ltd.). Pressures were measured by ruby luminescence.

Density functional theory (DFT) calculations have been performed using the QUANTUM ESPRESSO package [25]. The exchange correlation energy is determined using the generalized gradient density approximation (GGA) as parameterized by Perdew, Burke, and Ernzerhof [26]. The scalar and fully relativistic ultrasoft pseudopotentials [27,28] are used for inclusion of the interactions between ionic cores and valence electrons and the effects of SOC. The crystal structure at each pressure is obtained by optimizing the lattice constants and atomic coordinates through minimization of enthalpy. Phonon frequencies of all BiSe phases are estimated using density functional perturbation theory (DFPT) as implemented in the QUANTUM ESPRESSO code [29]. The SC $T_c$ is estimated within the BCS theory by calculating the Eliashberg spectral function and using the McMillan's equation [30]. The (001) surface of the cubic ($Pm\bar{3}m$) BiSe phase is modeled with a periodic supercell consisting of infinite slab and vacuum to determine the surface electronic states (see Supplemental Material [31]).

X-ray powder diffraction patterns of BiSe at various pressures are shown in Fig. 1(a). The ambient trigonal structure ($P\bar{3}m1$, $z = 6$) is stable up to 7.4 GPa. However, a closer look at the pressure variation of the trigonal $c/a$ ratio shows a change in slope near 3 GPa [Fig. 1(d)], indicating an isostructural transition, which is also supported by the change in bulk compressibility and the $p$ dependence of the Raman mode frequencies (see Supplemental Material [31]). At 7.8 GPa, the emergence of several new Bragg peaks indicates a structural phase transition. The trigonal phase, however, persists up to 9 GPa with decreasing phase fraction. The new peaks can be indexed as a combination of two orthorhombic phases, *Cmcm* and *Pnma* (GeS type). Similar tangled high-$p$ orthorhombic structures have been reported earlier for SnTe and SnSe compounds due to the closely matching enthalpy in these structures [32,33]. The emergence of new peaks
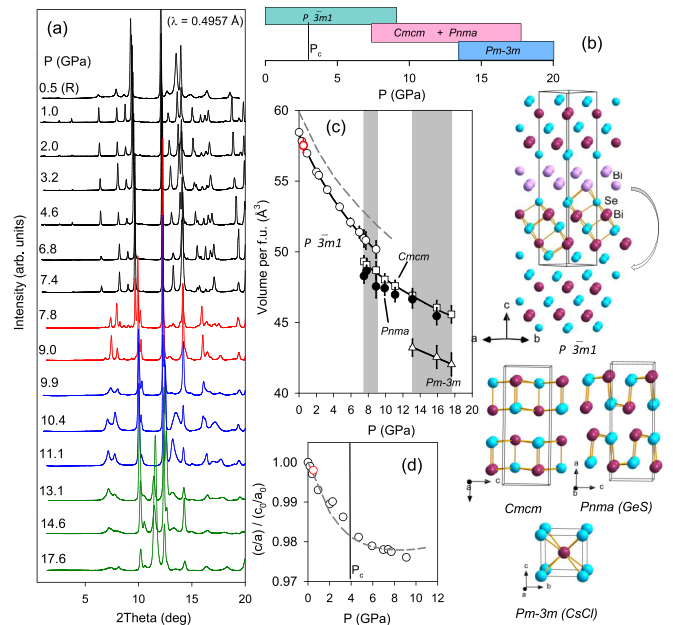


FIG. 1. (a) XRD patterns of BiSe at various pressures. The top pattern is at 0.5 GPa upon $p$ release, indicated by (R). (b) The phase transition sequence upon $p$ increase; the vertical line represents an isostructural transition at $P_c \sim 3$ GPa. Crystal structures are shown for different BiSe phases. Pressure variation of (c) volume per formula unit in different phases and (d) the $c/a$ ratio in the low-$p$ trigonal phase. Red open symbols represent the data upon $p$ release; theoretical results are shown by the dashed curve.

above 13 GPa has been indexed as the cubic BiSe phase ($Pm\bar{3}m$). The orthorhombic phase fraction rapidly decreases above 14.6 GPa, and the structural transition to the cubic phase is nearly completed at 17.6 GPa. The structural details are obtained by the Rietveld fit of the diffraction patterns up to 7.4 GPa, and the multiphase LeBail profile fits at higher pressures (see Supplemental Material [31]). Figure 1(c) shows the $p$ variation of volume per formula unit in different phases, highlighting the mixed phase regions. Figure 1(b) displays BiSe lattices and phase stability ranges; the trigonal structure first undergoes a complete atomic rearrangement into the orthorhombic structural motif, which upon $p$ increase evolves into the cubic structure. An enhanced structural disorder at high $p$ is apparent from the intrinsic broadened Bragg peaks. The Raman spectra show dramatic changes across the structural transitions (see Supplemental Material [31]). Although the structural transitions are reversible, the observed broad XRD peaks at 0.5 GPa upon $p$ release indicate the irreversible nature of structural disorder [see Fig. 1(a)].

The band structure calculations including SOC of the ambient trigonal ($P\bar{3}m1$) phase of BiSe reveal band inversion along the $\Gamma$-$A$ direction and opening of a band gap at all $k$ vectors in the Brillouin zone (see Supplemental Material [31]). An analysis based on the Fu-Kane method [3] confirms the weak topological insulator state [$Z_2$ invariant (0;001)] with an indirect band gap of 11 meV. Figure 2(a) shows the pressure variation of the calculated enthalpy $\Delta H$ of the orthorhombic and cubic phases with respect to the trigonal phase of BiSe. $\Delta H$ of the orthorhombic phases (*Cmcm* and *Pnma*) decrease monotonically and eventually becomes negative near 10 GPa,
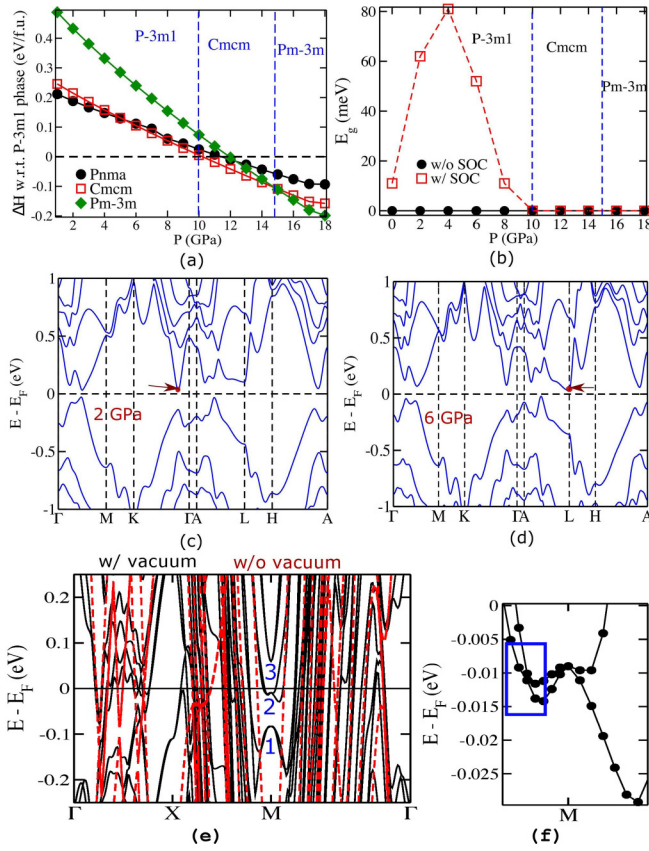
FIG. 2. (a) Pressure-dependent enthalpy difference (per formula unit) $\Delta H$ of orthorhombic *Pnma*, *Cmcm*, and cubic *Pm$\bar{3}$m* BiSe phases with respect to the *P$\bar{3}$m1* phase. (b) Pressure variation of the band gap as calculated with and without SOC. Electronic structure (with SOC) of the *P$\bar{3}$m1* phase at (c) 2 GPa and (d) 6 GPa. Changes in the positions of the conduction band minima, marked by red arrows in (c) and (d), explain the anomalous pressure dependence of the band gap in (b). (e) Comparison of electronic structures (with SOC) of the $1 \times 1 \times 10$ supercell of the *Pm$\bar{3}$m* phase with 15 Å vacuum along the *c* axis and that without vacuum. Three doubly degenerate surface states near the *M* point are denoted by 1, 2, and 3. (f) Linear band crossing is seen for band 2 at 12 meV below the Fermi level.

confirming the structural transition to the orthorhombic phase. Although the *Cmcm* phase is energetically favorable in the *p* range of 10–15 GPa, the *Pnma* phase, having closely matching enthalpy, can be kinetically stable near 10 GPa at room temperature, in accordance with our XRD results. The enthalpy variation also supports the stability of the cubic (*Pm$\bar{3}$m*) phase above 15 GPa. The *p* variation of the estimated lattice parameters of the *P$\bar{3}$m1* phase shows an anomaly at 4.5 GPa, agreeing with the observed isostructural transition [see Fig. 1(c)]. This has also been evident from the changes in *p* coefficients of the calculated Raman mode frequencies, in agreement with Raman studies (see Supplemental Material [31]). It may be noted that the structural transition pressures have been overestimated by ∼2 GPa in our DFT calculations. The smallest (indirect) band gap of the trigonal phase increases to 80 meV at 4 GPa, beyond which it decreases and eventually vanishes at 10 GPa [Fig. 2(b)]. Such reversal trend of the band gap above 4 GPa results from the change in conduction band minimum from the $\Gamma$-*K* direction to the *L*
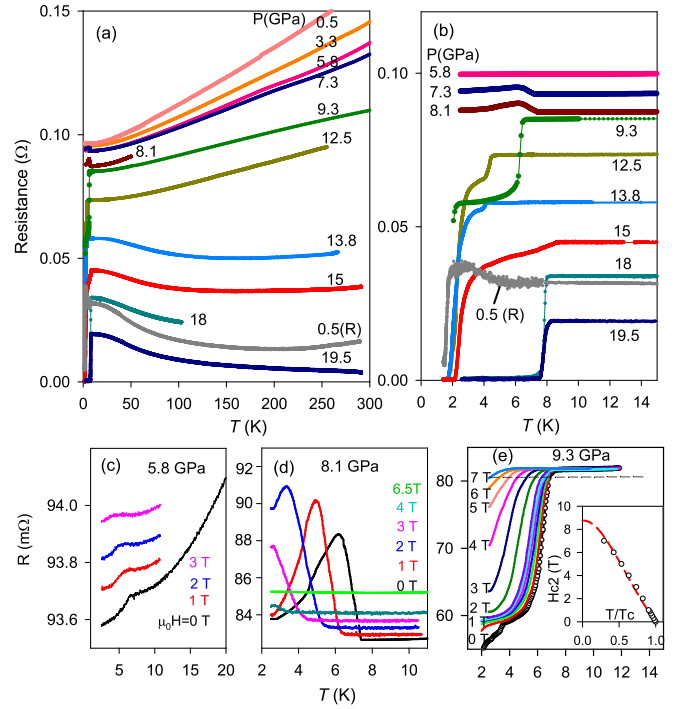


FIG. 3. (a) Resistance of BiSe plotted as a function of temperature at various pressures. The plot marked 0.5(R) is at 0.5 GPa upon *p* release. Resistance is measured in the *ab* plane of the trigonal structure. (b) $R(T)$ plots near the SC transition above 5.8 GPa. Magnetic field variation of the $R(T)$ plots near the SC transition at (c) 5.8 GPa, (d) 8.1 GPa, and (e) 9.3 GPa. The inset in (e) shows the $T_c$-$H$ data plot at 9.3 GPa and the Ginzburg-Landau fit.

point of the Brillouin zone (BZ) [Figs. 2(c) and 2(d)]. The indirect-indirect band-gap crossover can be associated with the observed isostructural transition. Analysis shows that the weak topological insulator state [with $Z_2$ invariants (0;001)] remains unchanged in the gapped state and BiSe becomes metallic above 10 GPa. Our supercell calculation for an infinite slab of the *Pm$\bar{3}$m* phase with vacuum interface shows the emergence of doubly degenerate surface bands with linear crossing near the Fermi level, revealing the topological nature [see Figs. 2(e) and 2(f)], whereas the metallic orthorhombic phases (*Cmcm* and *Pnma*) are found topologically trivial.

Single-crystal BiSe usually grow as highly *n* doped due to Se vacancies [24], displaying large bulk metallic conduction, as in the case of $Bi_2Se_3$ [34]. Figure 3(a) shows *T*-dependent resistance plots at various pressures. The overall $R(T)$ behavior changes only marginally up to 8.1 GPa, except at low temperatures. A resistance peak feature is observed below 8 K at 7.3 and 8.1 GPa [see Fig. 3(b)]. The magnetic field dependence [Fig. 3(d)] and current variation measurements (see Supplemental Material [31]) suggest this feature to be associated with the onset of SC domains. The peak feature near the onset of the SC transition and also two-step transitions have been presented earlier for many layered topological insulators [22,35–37]. The detailed investigations of boron-doped diamond have revealed that the resistance peak or two-step transitions originate from the formation of bosonic islands at the SC onset and subsequently achieving the percolation threshold at a lower temperature, initiating a resistance drop

[38,39]. This is attributed to the granularity (intrinsic and extrinsic) of the emerged SC domains. As the SC in BiSe appears near the border of the structural transition, it is suggested that bulk SC emerges in the orthorhombic phases. The onset $T_c$s are determined from the peak positions in the $dR/dT$ plots (see Supplemental Material [31]). At 5.8 GPa, the observed resistance anomaly near 7 K is also assigned to the onset of filamentary SC, based on the observed field dependence [Fig. 3(c)].

At 9.3 GPa, the resistance drops significantly in two steps at 6.8 and 2 K [Fig. 3(b)]. The large separation between the steps hints that the feature arises due to the two coexisting SC phases with distinct $T_c$s, as supported by our theoretical estimation; the $Cmcm$ phase has higher $T_c$ than $Pnma$. While the first step is due to SC onset of the $Cmcm$ phase, the broad hump-shaped resistance drop at lower $T$ for $p$ up to 13.8 GPa corresponds to the SC onset of the $Pnma$ phase. In a second measurement (Run2), a two-step and bumplike resistance anomaly with zero resistance at 1.4 K is observed at 8.5 GPa, indicating a large fraction of the $Pnma$ phase at this pressure (see Supplemental Material [31]). The magnetic field dependence of the $R(T)$ curve at 9.3 GPa shows that the onset $T_{c1}$ of the $Cmcm$ phase decreases systematically with increasing field [see Fig. 3(e)]. At a field of 7 T, the SC transition almost smears out. The $T_c$-$H$ plot, when fitted with the Ginzburg-Landau (GL) equation $H_{c2}=H_{c2}(0)[(1-t^2)/(1+t^2)]$, where t=$T/T_c$, estimates the upper critical field $H_{c2}(0) \sim 8.7$ T for the $Cmcm$ phase. This is well below the BCS weak-coupling Pauli limit of $H_p = 1.86 * T_c$ (0) = 12.6 T. $H_{c2}(0)$ has been estimated as $\sim 3$ T for the $Pnma$ phase from the field variation of the second onset $T_{c2}$ at 12.5 GPa. At pressures above 12.5 GPa, the $R(T)$ curves change drastically. An unconventional metallic behavior ($dR/dT < 0$) is observed below 150 K, possibly due to $p$-induced structural disorder, as evident from XRD peak broadening. The distinct sharp resistance drop below 8 K at 18 GPa is associated with the high-$p$ cubic BiSe phase, as the $Cmcm$ to $Pm\bar{3}m$ structural transition is nearly completed at this pressure. At 15 GPa, a clear resistance anomaly at 8 K is due to the presence of a small fraction of the $Pm\bar{3}m$ phase. Upon $p$ release, unconventional metallic $R(T)$ persists at 0.5 GPa [see Fig. 3(a)] and, more importantly, SC is preserved with $T_c \sim 2$ K [Fig. 3(b)]. The observed SC is assigned to the ambient trigonal phase and the enhanced structural disorder is believed to be responsible for the unconventional metallic nature in its normal state. The emergence of SC in the ambient trigonal phase by $p$ cycling provides a different route to explore topological SC.

The pressure variation of SC $T_c$ is summarized in Fig. 4(a). The onset $T_c$ shows a dome-shaped behavior in the $Cmcm$ phase. With the emergence of the $Pm\bar{3}m$ phase, $T_c$ increases abruptly to 8 K and remains mostly unchanged with $p$ increase. The distinct $p$ variations of $T_c$ and the SC transition width help assign distinct SC phases with different structures. The bulk nature of SC in the high-pressure phases is evident from the observed diamagnetic response in the dc-susceptibility measurements [Fig. 4(b)]. Our calculated Eliashberg spectral functions indicate that the optical phonons at high-symmetry points couple strongly with the electronic states (see Supplemental Material [31]). The estimated $T_c$s are 6 and 4.2 K in the $Cmcm$ and $Pnma$ phases, respectively, at
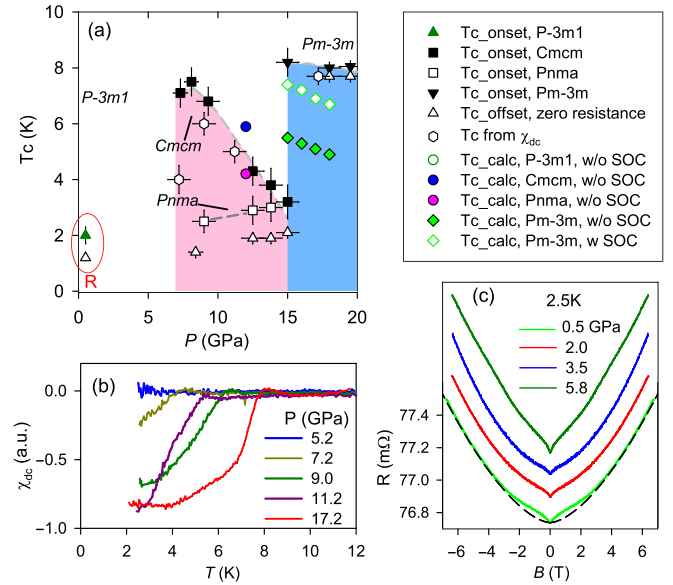


FIG. 4. (a) Pressure variation of SC $T_c$ (from experiment and theory); $p$ ranges for distinct phases are shown shaded. Symbols are explained in the legend box. (b) Zero-field-cooled (ZFC) dc-susceptibility data at 50 Oe field at high pressures. (c) In-plane resistance of the trigonal BiSe phase at 2.5 K as a function of field at various pressures. The resistance scale is shown for the curve at 0.5 GPa. The curves for higher $p$ are arbitrarily shifted for clear comparison of low-field WAL features. The dashed line at 0.5 GPa is the power-law fit of the high-field MR data.

12 GPa. The electron-phonon coupling (EPC) constant in the $Cmcm$ phase decreases rapidly with increasing pressure by mode stiffening, resulting in the $p$-induced decrease of $T_c$, in agreement with experiments. In the $Pm\bar{3}m$ phase at 18 GPa, estimated $T_c = 4.8$ K. The observed enhanced $T_c(\sim 8$ K) can be understood in terms of the effect of SOC that enhances the EPC due to the increased phonon linewidth, which is in agreement with the Raman results (see Supplemental Material [31]). The prediction of the topological surface states and the observed bulk SC identify the $Pm\bar{3}m$ BiSe phase as a candidate for topological SC. The unusual $p$-independent $T_c$ in this phase indicates the possible unconventional nature of SC, which warrants further investigations at higher field.

We estimate the SC $T_c = 0.3$ K (without SOC) in the trigonal ($P\bar{3}m1$) phase at 6 GPa. Based on our theoretical understanding of the cubic BiSe phase, we justify the observed resistance drop at 5.8 GPa with possible onset of filamentary SC below $\sim 7$ K as originated from the enhanced EPC due to SOC-induced phonon linewidth broadening. This is supported by the observed abrupt and irreversible broadening of the Raman spectra above 6 GPa. The signature of the strong SOC in the $P\bar{3}m1$ phase is clearly evident from the field-dependent in-plane resistance plots [Fig. 4(c)]. The cusplike enhanced positive magneto-resistance at low field is due to weak antilocalization (WAL). The quantum correction to the bulk conductivity in this WTI occurs due to the strong SOC-induced formation of spin-polarized Rashba states on its (001) plane [14,24]. The prominent WAL feature has been observed in the $R(B)$ plot at 5.8 GPa. In the case of the $p$-released sample, the enhanced structural disorder (as evident from

XRD) add additional phonon linewidth broadening (seen in the Raman spectra), causing further enhancement of the EPC and so increased SC $T_c$. While zero resistance clearly indicate SC transition, nonobservation of the diamagnetic response at 2 K may be due to the small SC volume fraction; however, the possibility of surface-state linked superconductivity cannot be ruled out. The above results thus encourage further experimental and theoretical investigations to understand the role of SOC in the emerged SC and the topological nature in the $p$-released sample.

[1] L. Fu and C. L. Kane, Phys. Rev. Lett. **100**, 096407 (2008).

[2] M. Z. Hasan and C. L. Kane, Rev. Mod. Phys. **82**, 3045 (2010).

[3] L. Fu and C. L. Kane, Phys. Rev. B **76**, 045302 (2007).

[4] Y. Xia, D. Qian, D. Hsieh, L. Wray, A. Pal, H. Lin, A. Bansil, D. Grauer, Y. S. Hor, R. J. Cava *et al.*, Nat. Phys. **5**, 398 (2009).

[5] H. Zhang, C.-X. Liu, X.-L. Qi, X. Dai, Z. Fang, and S.-C. Zhang, Nat. Phys. **5**, 438 (2009).

[6] B. Rasche, A. Isaeva, M. Ruck, S. Borisenko, V. Zabolotnyy, B. Büchner, K. Koepernik, C. Ortix, M. Richter, and J. van den Brink, Nat. Mater. **12**, 422 (2013).

[7] R. Noguchi, T. Takahashi, K. Kuroda, M. Ochi, T. Shirasawa, M. Sakano, C. Bareille, M. Nakayama, M. D. Watson, K. Yaji *et al.*, Nature (London) **566**, 518 (2019).

[8] N. Avraham, A. K. Nayak, A. Steinbok, A. Norris, H. Fu, Y. Sun, Y. Qi, L. Pan, A. Isaeva, A. Zeugner *et al.*, Nat. Mater. **19**, 610 (2020).

[9] P. Zhang, R. Noguchi, K. Kuroda, C. Lin, K. Kawaguchi, K. Yaji, A. Harasawa, M. Lippmaa, S. Nie, H. Weng *et al.*, Nat. Commun. **12**, 406 (2021).

[10] K. Lee, G. F. Lange, L.-L. Wang, B. Kuthanazhi, T. V. Trevisan, N. H. Jo, B. Schrunk, P. P. Orth, R.-J. Slager, P. C.Canfield *et al.*, Nat. Commun. **12**, 1855 (2021).

[11] L. Fu, Phys. Rev. Lett. **106**, 106802 (2011).

[12] Y. Tanaka, Z. Ren, T. Sato, K. Nakayama, S. Souma, T. Takahashi, K. Segawa, and Y. Ando, Nat. Phys. **8**, 800 (2012).

[13] R.-J. Slager, A. Mesaros, V. Juricic, and J. Zaanen, Nat. Phys. **9**, 98 (2013).

[14] M. Eschbach, M. Lanius, C. Niu, E. Mlynczak, P. Gospodaric, J. Kellner, P. Schuffelgen, M. Gehlmann, S. Doring, E. Neumann *et al.*, Nat. Commun. **8**, 14976 (2016).

[15] A. J. Liang, J. Jiang, M. X. Wang, Y. Sun, N. Kumar, C. Shekhar, C. Chen, H. Peng, C. W. Wang, X. Xu *et al.*, Phys. Rev. B **96**, 165143 (2017).

[16] F. Schindler, A. M. Cook, M. G. Vergniory, Z. Wang, S. S. P. P. B. A. Bernevig, and T. Neupert, Sci. Adv. **4**, eaat0346 (2018).

[17] J. Langbehn, Y. Peng, L. Trifunovic, F. von Oppen, and P. W. Brouwer, Phys. Rev. Lett. **119**, 246401 (2017).

[18] P. Zareapour, A. Hayat, S. Y. F. Zhao, M. Kreshchuk, A. Jain, D. C. Kwok, N. Lee, S.-W. Cheong, Z. Xu, A. Yang *et al.*, Nat. Commun. **3**, 1056 (2012).

[19] F. Yang, Y. Ding, F. Qu, J. Shen, J. Chen, Z. Wei, Z. Ji, G. Liu, J. Fan, C. Yang *et al.*, Phys. Rev. B **85**, 104508 (2012).

[20] Y. S. Hor, A. J. Williams, J. G. Checkelsky, P. Roushan, J. Seo, Q. Xu, H. W. Zandbergen, A. Yazdani, N. P. Ong, and R. J. Cava, Phys. Rev. Lett. **104**, 057001 (2010).

[21] S. Sasaki, M. Kriener, K. Segawa, K. Yada, Y. Tanaka, M. Sato, and Y. Ando, Phys. Rev. Lett. **107**, 217001 (2011).

[22] K. Kirshenbaum, P. S. Syers, A. P. Hope, N. P. Butch, J. R. Jeffries, S. T. Weir, J. J. Hamlin, M. B. Maple, Y. K. Vohra, and J. Paglione, Phys. Rev. Lett. **111**, 087001 (2013).

[23] K. Matsubayashi, T. Terai, J. S. Zhou, and Y. Uwatoko, Phys. Rev. B **90**, 125126 (2014).

[24] K. Majhi, K. Pal, H. Lohani, A. Banerjee, P. Mishra, A. K. Yadav, R. Ganesan, B. R. Sekhar, U. V. Waghmare, and P. S. A. Kumar, Appl. Phys. Lett. **110**, 162102 (2017).

[25] P. Giannozzi, S. Baroni, N. Bonini, M. Calandra, R. Car, C. Cavazzoni, D. Ceresoli, G. L. Chiarotti, M. Cococcioni, I. Dabo *et al.*, J. Phys.: Condens. Matter **21**, 395502 (2009).

[26] J. P. Perdew, K. Burke, and M. Ernzerhof, Phys. Rev. Lett. **77**, 3865 (1996).

[27] D. Vanderbilt, Phys. Rev. B **41**, 7892 (1990).

[28] A. Dal Corso and A. Mosca Conte, Phys. Rev. B **71**, 115106 (2005).

[29] S. Baroni, S. de Gironcoli, A. D. Corso, and P. Giannozzi, Rev. Mod. Phys. **73**, 515 (2001).

[30] W. L. McMillan, Phys. Rev. **167**, 331 (1968).

[31] See Supplemental Material at http://link.aps.org/supplemental/10.1103/PhysRevB.107.024506 for additional data, figures of high-pressure x-ray diffraction, Raman, resistance, magnetoresistance measurements, and theoretical calculations.

[32] D. Zhou, Q. Li, Y. Ma, Q. Cui, and C. Chen, J. Phys. Chem. C **117**, 5352 (2013).

[33] D. Zhou, Q. Li, W. Zheng, Y. Mac, and C. Chen, Phys. Chem. Chem. Phys. **19**, 4560 (2017).

[34] J. G. Checkelsky, Y. S. Hor, M.-H. Liu, D.-X. Qu, R. J. Cava, and N. P. Ong, Phys. Rev. Lett. **103**, 246601 (2009).

[35] Y. Qi, W. Shi, P. G. Naumov, N. Kumar, R. Sankar, W. Schnelle, C. Shekhar, F.-C. Chou, C. Felser, B. Yan *et al.*, Adv. Mater. **29**, 1605965 (2017).

[36] X. Li, D. Chen, M. Jin, D. Ma, Y. Ge, J. Sun, W. Guo, H. Sun, J. Han, W. Xiao *et al.*, Proc. Natl. Acad. Sci. USA **116**, 17696 (2019).

[37] Y. Zhou, J. Wu, W. Ning, N. Li, Y. Du, X. Chen, R. Zhang, Z. Chi, X. Wang, X. Zhu *et al.*, Proc. Natl. Acad. Sci. USA **113**, 2904 (2016).

[38] G. Zhang, M. Zeleznik, J. Vanacken, P. W. May, and V. V. Moshchalkov, Phys. Rev. Lett. **110**, 077001 (2013).

[39] G. Zhang, T. Samuely, J. Kacmarcik, E. A. Ekimov, J. Li, J. Vanacken, P. Szabo, J. Huang, P. J. Pereira, D. Cerbu *et al.*, Phys. Rev. Appl. **6**, 064011 (2016).